Journal of Renewable Materials
DOI:10.32604/jrm.2020.012808
Article

Tech Science Press

The Influence of Two Natural Reinforcement Fibers on the Hygrothermal Properties of Earthen Plasters in Mogao Grottoes of China

Wenbei Bi[1], Zengfeng Yan[1,*], Huan Zhao[1], Lixin Sun[2], Xudong Wang[3,4] and Zhengmo Zhang[3]

[1]School of Architecture, Xi'an University of Architecture and Technology, Xi'an, 710055, China
[2]China Academy of Building Research, Beijing, 100044, China
[3]Conservation Institute, Dunhuang Academy, Dunhuang, 736200, China
[4]School of Engineering and Mechanics, Lanzhou University, Lanzhou, 730000, China
[*]Corresponding Author: Zengfeng Yan. Email: xazfyan@126.com
Received: 13 July 2020; Accepted: 26 August 2020

Abstract: Murals in Mogao Grottoes consist of three parts: support layer, earthen plasters and paint layer. The earthen plasters play a key role in the preservation of murals. It is a mixture of Dengban soil, sand, and plant fiber. Two different natural fibers, hemp fiber and cotton fiber, were reinforced to earthen plasters in the same percentage to evaluate the influence on hygrothermal performance. The two types of earthen plasters were studied: one containing hemp fiber in the fine plaster (HFP) and the other containing cotton fiber in the fine plaster (CFP). Specific heat capacity, dry thermal conductivity, water vapor permeability, and sorption isotherms were investigated. The results showed that the difference between two natural fibers has much more impact on the hygric properties (water vapor permeability and sorption isotherms) of earthen plasters than on their thermal performance (specific heat capacity and dry thermal conductivity). The CFP with higher density has higher thermal conductivity than the HFP with lower density. But no significant differences of specific heat capacity were observed. Compared with HFP, CFP used in murals can reduce the rate of water transfer and prevent salt from transferring water to the mural surface. The overall findings highlight that all these features of CFP are beneficial to the long-term preservation of murals. The study of the earthen plasters in Mogao Grottoes is of general significance, and the measured properties can be used to obtain coupled heat and moisture analysis of the earthen plasters and to dissect the degradation mechanism of murals.

Keywords: Earthen plasters; natural reinforced fibers; hygrothermal properties; dry thermal conductivity; water vapor permeability; sorption isotherms

1 Introduction

Mogao Grottoes in Dunhuang, China, a UNESCO World Heritage Site with invaluable murals and sculptures dating back to the 4th century A.D.–14th century A.D., represents the highest artistic and technical achievement in the Silk Road [1]. There are 492 caves in Mogao grottoes, with 45,000 square meters of murals and 2,415 painted sculptures. The murals in Mogao grottoes are of high artistic value, consisting of three parts: support layer (conglomerate), earthen plasters, and paint layer (Fig. 1).

Protection work is routinely needed to maintain a long-term stable and interdependent condition among the paint layer, earthen plasters, and support layer.

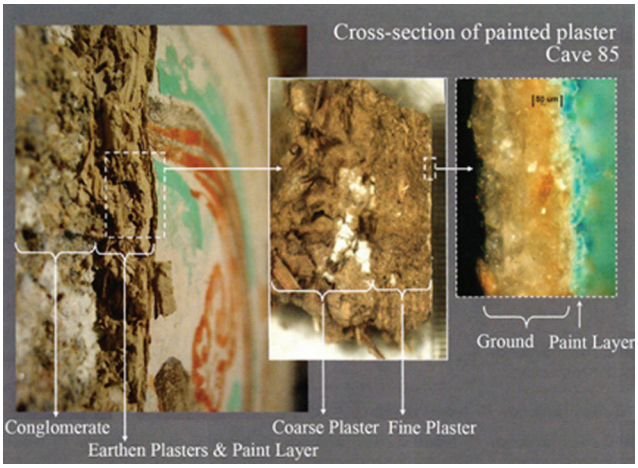

Figure 1: Stratigraphy of murals in Mogao Grottoes. Credit: J. Paul Getty Trust

Commonly, earthen plaster is used to create a flat surface that readily accommodates paint. As a kind of earth-based materials with reinforced fibers, earthen plaster has the advantages of easy-to-use, low price, and a great capacity to adjust indoor air temperature and humidity [2]. With a proper combination of heat storage and humidity control, earthen walls can improve the indoor thermal environment, as well as the indoor comfort [3,4]. Natural materials such as coconut fibers [5], hemp [6], straw [7], flax fibers [8], olive fibers [9], and bamboo [10], have always been used as reinforced fibers in composite materials. Many of their characteristics have already been studied, including good mechanical properties, low cost, low density, low thermal conductivity, durability, and recyclability. The hemp-lime plasters used in residential buildings were found to be hygroscopic and breathable materials, which has relatively low thermal conductivity (around 0.2 W/m.K) and a moisture penetration depth of about 6–7 cm [11].

Earthen plasters used in ancient murals is also a composite material with natural fibers being added to prevent excessive cracking under dry conditions. In Mogao Grottoes, the earthen plasters is a mixture of Dengban soil, sand, and plant fiber (like wheat straw, hemp, or cotton) [12], which comprises two different earthen layers: base layer (wheat straw plaster) and the upper layer (hemp or cotton plaster). The thick and long fiber added in the base layer aims to strengthen the connectivity between the earthen plasters and conglomerate, and to build up the strength of plasters [13]. There are two types of earthen plasters used in Mogao murals according to the different fiber reinforced in the upper layer. The coarse plasters of the two earthen plasters were the same: both were reinforced with wheat straw. As for the fine plasters, two different fibers-hemp fiber and cotton fiber-were used. Hemp and cotton fibers have been tested as reinforce-ment agents in bio composites [14–18]. The hygrothermal behavior of the two fibers varies significantly because of their different physical structure and chemical composition [19]. The cellulose content of hemp fiber is about 70%, the content of hemicellulose, and lignin comes second after cellulose. The content of lignin is as high as 14%, resulting in rough and hard fibers. Hemp fiber has fast moisture absorption and moisture releasing speed. The moisture regain rate is about 14% under general atmospheric conditions, so the fabrics are cool and comfortable to wear in summer. The main component of cotton fiber is cellulose, which comprises 94%, and the rest is associated cellular organisms. There are many hydrophilicity genes on the cellulose macromolecules, which have good hygroscopicity. Under general atmospheric conditions, the moisture regain rate of cotton fiber can reach 8.5% [20,21].

It is extremely important to have proper knowledge of the earthen plasters as it is the root of many problems associated with the conservation of decorative surfaces [22]. Fig. 2 shows the photos of the earthen plasters and paint layer. Fig. 2 shows images of the earthen plaster and paint layer. Based on currently available data, earthen plaster is used as the cohesion and adhesion base layers of the conglomerate and painting layer [12]. Plaster detachment and soil disruption play crucial roles in wall-painting destruction. When salinity occurs in the interior of the earthen plasters surface polymerization, it can make the earthen plasters swell and fall off, or make the earthen plasters gradually scatter. Once this disorder occurs, it will be difficult to control, and eventually lead to the paint layer peeling off, resulting in the destruction of the mural [23]. In the field of restoration, this type of building material has specific advantages over traditional ones, especially in certain environments. It plays a key role in the preservation of murals. In the early and middle Tang dynasty, the craftsmanship of the earthen plasters was virtuoso, and the level of mural painting reached its peak in Mogao Grottoes. During this period, the earthen plasters were relatively thick, and the main disease of murals was the discoloration and fading of the paint layer. While in the late Tang dynasty, the craftsmanship of the earthen plasters became more mediocre, and the thickness of the earthen plasters was attenuated, even as thin as less than one millimeter. Without the earthen plasters, the salt in the conglomerate could infiltrate more easily and cause efflorescence to murals.

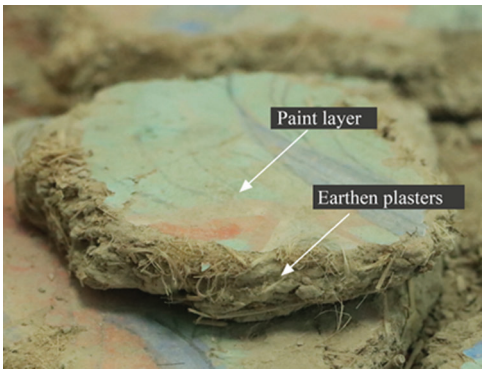

Figure 2: The photos of the earthen plasters and paint layer

Over the past thousands of years, vulnerable murals have suffered various damages caused by different microenvironments and human activities [24,25]. The disease of salt efflorescence is the result of interaction among thermal, moisture and salt. Previous studies have focused more on the impact of salt or water. Research into the thermal and moisture properties of the earthen plasters may provide a theoretical basis for investigating the deterioration incurred in wall paintings.

In Mogao Grottoes, soluble salts (mainly sodium chloride and sodium sulfate) can cause the disease of salt efflorescence through cycles of deliquescence and recrystallization after migration from the rock in and on the painted plaster [26]. The relationship between humidity and soluble salts has been well known [27,28], but the coupling effect of heat and moisture is elusive. A real-time monitoring system has been installed in Mogao Grottoes to collect various data, such as temperature, RH, and wind speed [29]. Characterization of spatial distribution regularities of water vapor and salt in caves helped to establish the relationship between temperature, RH, and salt [30]. As a great cause of moisture and salt migration, temperature gradient merits special attention based on the analysis of the data of temperature and RH inside and outside the cave [31]. In the long term, the environmental control of caves at risk should be the preferred damage mitigation method [23]. Conservation treatments require a better understanding of the cause-and-effect relationship between thermal, moisture and salts and, preferably, in detail, including rates of hygrothermal-mediated

deterioration. Since the process of coupling thermal and moisture is directly influenced by the properties of the earthen plasters, the hygrothermal characteristics of the earthen plasters should be analyzed in detail.

More attention has been paid to the mechanical, chemical and mineralogical properties of the earthen plasters in murals [32,33]. Only a few studies have investigated their hygrothermal properties, especially in ancient cultural relics [30]. Investigation on the hygrothermal properties of the earthen plasters helps to gain a better understanding of the heat and moisture transport in wall paintings, and also lays a foundation for further studying the interaction between heat, moisture, and salt.

This study aims to assess the influence of two natural reinforced fibers on the hygrothermal performance of earthen plaster samples. Their dry thermal conductivity, specific heat capacity, water vapor permeability, and moisture sorption isotherm were characterized. The overall findings provided detailed information on the hygrothermal properties of the earthen plasters and laid a theoretical basis for investigating the deterioration of wall paintings and determining the environmental parameter thresholds in the caves. Ultimately, knowledge gleaned from this study is conducive to the development of methods for the preventive conservation of wall paintings.

2 Materials

2.1 Raw Materials

The earthen plasters of Dunhuang murals has a multi-layer composite structure consisting of coarse plaster and fine plaster. The schematic diagram of the earthen plasters in Mogao Grottoes is shown in Fig. 3. The natural reinforced fibers used in this study were hemp fiber and cotton fiber. To simulate the original composition of wall paintings, two kinds of specimens were prepared and tested (Tab. 1). The coarse plasters of these two specimens were the same: both were reinforced with wheat straw. As for the fine plasters, two different fibers-hemp fiber (HFP) and cotton fiber (CFP)-were used.

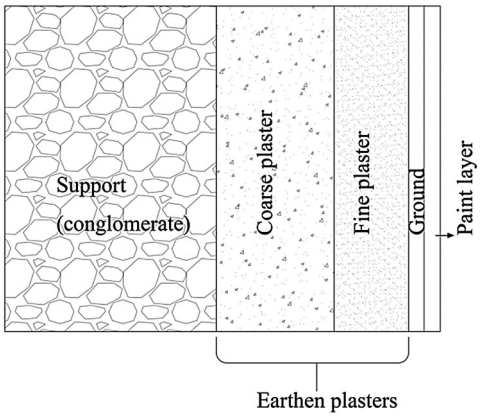

Figure 3: Schematic diagram of the earthen plasters in Mogao Grottoes

The clayey soil was obtained from a location in Daquan River in front of Mogao Grottoes, called Dengban soil locally. The Dengban-soil-to-sand ratio of 64:36 was used [12]. The sand was collected in the riverbed of Daquan River. Fibers were added in these samples to improve the toughness. Wheat straw, hemp, and cotton were collected from Dunhuang. Dengban soil and sand were dried to a constant weight in an oven at 110°C before being used to fabricate earthen plaster samples. Fibers were thumped for half an hour for softening and cut to chips of less than 1 cm. Raw materials used for preparing earthen plaster samples are shown in Fig. 4. Moreover, hemp fiber and cotton fiber also present important differences regarding their microstructure, which is visible on the scanning electron microscope (SEM)

pictures (Fig. 5). The cross-section of hemp fiber is a fiber bundle that is composed of many irregular polygonal fiber cells. A narrow middle layer separates the single fibers, and the middle cell lumen is oval-shaped. The fibrous cells of hemp fibers are long and slender, with closed ends and cell lumen. The cotton fiber is longitudinal in the shape of a flat tortuous ribbon, with an irregular waist round shape at the cross-section and cell lumens. The hemp fiber has a layered structure in the longitudinal direction.

Table 1: Compositions of earthen plaster samples

Notation	Composition					
	Dengban soil (wt%)	Sand (wt%)	Additive (wt%)			Water (wt%)
			Wheat straw	Hemp	Cotton	
HFP	Coarse plaster	64	36	3	——	—— 20
	Fine Plaster	64	36	——	3	—— 20
CFP	Coarse plaster	64	36	3	——	—— 20
	Fine Plaster	64	36	——	——	3 20

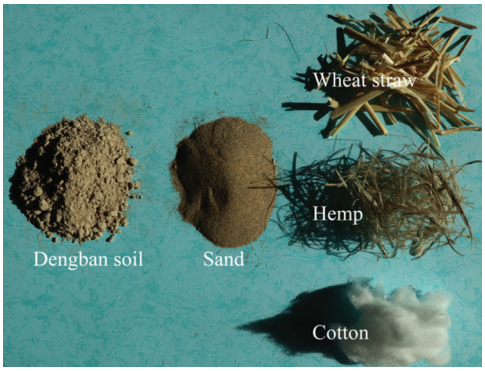

Figure 4: Raw materials for preparing earthen plaster samples

The granulometric curve of Dengban soil and sand are presented in Fig. 6. The composition of the Dengban soil is 37% clay (less than 5 μm), 55% silt (between 5 and 50 μm) and 8% sand-sized particles (between 50 and 2000 μm). The Dengban soil and sand of Mogao based on the sand, silt, and clay proportions were plotted on the sand–silt–clay ternary diagram (United States, Department of Agriculture, USDA Textural Classification Chart), as shown in Fig. 7.

The X-ray Diffraction (XRD) data were analyzed for the identification of mineral phases by the Empyrean X-ray Diffraction system. The XRD analysis results are presented in Fig. 8. The main compositions of Dengban soil were quartz and chlorite, with others in less amount, such as illite, albite, muscovite, microcline, and calcite. The main compositions of sands were quartz with a smaller content of albite, muscovite, chlorite, and calcite. Besides, to determine the chemical compositions of Dengban soil and sand, an X-ray Fluorescence spectroscopy (XRF) was used. It was observed from the results (Tab. 2) that a higher amount of alum inosilicate minerals was contained. For example, the aluminum oxide in the Dengban soil and sand was 13.63% and 7.32%, respectively, while the corresponding silicate was, respectively, 42.7 and 51.66. A less percentage of calcium oxide was also observed in both the Dengban soil and sand. The results were in good agreement with the XRD data.

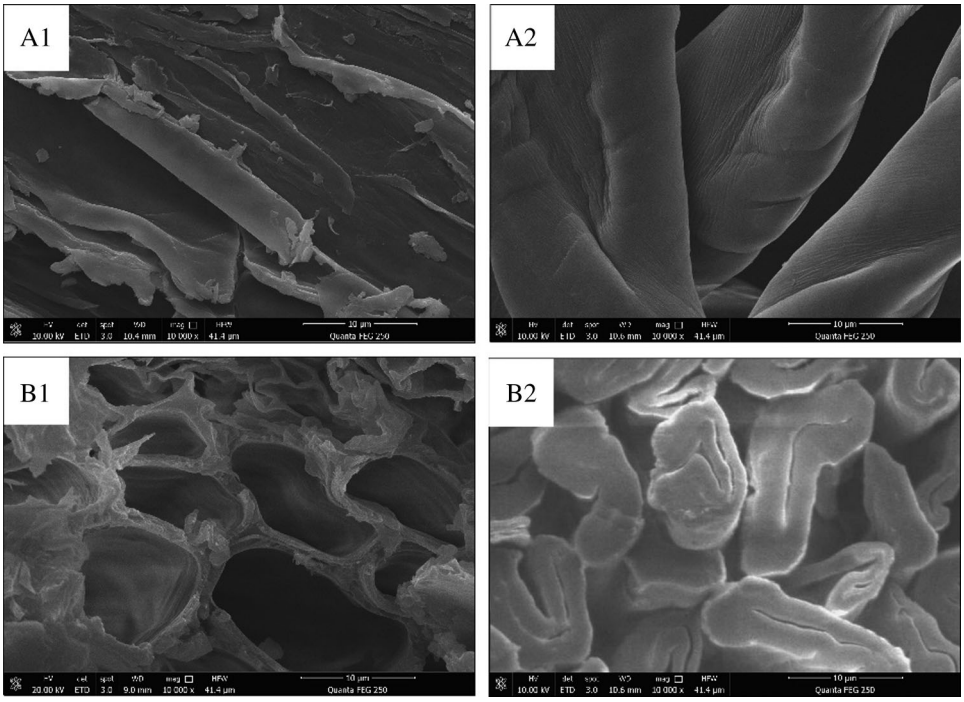

Figure 5: SEM images with the longitudinal section and the cross section of the hemp fiber (A1 and B1) and cotton fiber (A2 and B2)

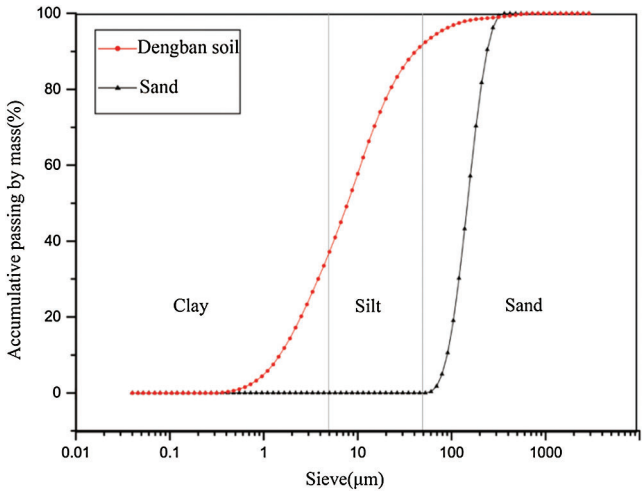

Figure 6: Granulometric study of Dengban soil and sand

2.2 Sample Preparation

These earthen plaster samples were produced using a traditional method. In Mogao Grottoes, cave temples were excavated into the cliff face, which is composed of conglomerate rock. The walls were then plastered and smoothed over with the earthen plasters and then painted with inorganic and organic pigments. A typical earthen plaster sample consists of two parts: a coarse plaster (the ground layer) and a fine plaster (the upper layer). Solid components in Tab. 1 were first mixed, followed by the addition of water. The coarse plaster was evenly placed in the mold, flattened to a thickness of 10 mm, and placed in

an oven at 60°C for 5 h. Then the surface of the dried coarse plaster was scratched and roughened with a knife (for better integration with the fine plaster). A fine plaster with a thickness of 5 mm was applied on the coarse plaster. After the production was completed, the sample was dried at 60°C for over 10 h. All samples were kept in a drying cabinet before testing. Samples with different dimensions were prepared for different tests: 15 × 15 × 1.5 cm for measuring water content, 30 × 30 × 3 cm for measuring dry thermal conductivity using the guarded hot plate method, and 5 × 5 × 1 cm for testing water vapor permeability and measuring sorption isotherms. Finally, the samples were granulated into powders with a particle size of smaller than 0.2 cm for the specific heat capacity measurements.

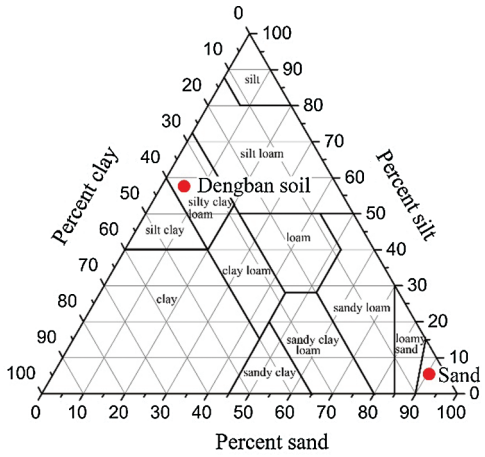

Figure 7: Ternary composition diagram of the Dengban soil and sand

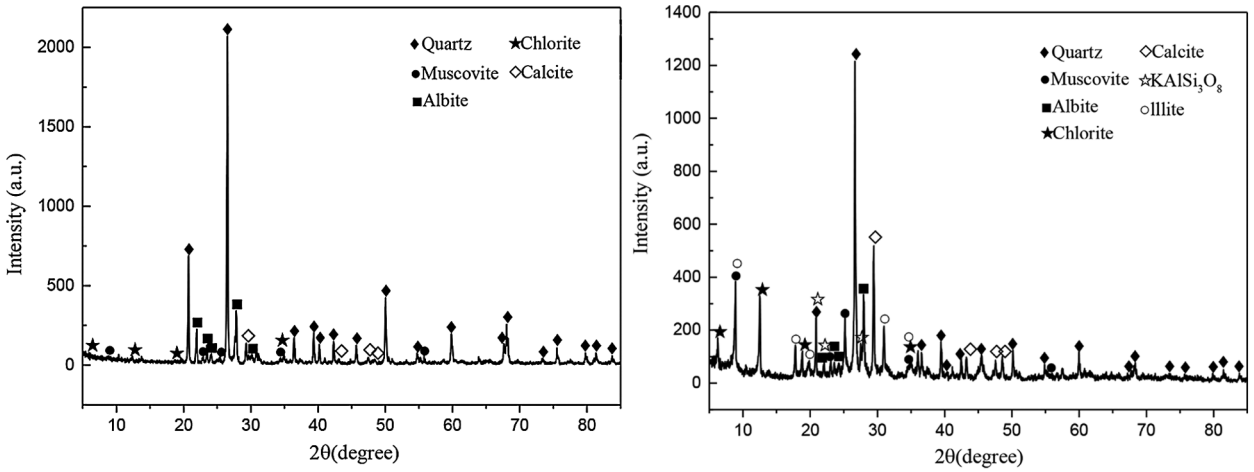

Figure 8: X-ray diffraction spectra of (a) Dengban soil and (b) sand

Table 2: Chemical compositions (% by weight) of raw materials by XRF

	SiO_2	Al_2O_3	CaO	Fe_2O_3	MgO	K_2O	Na_2O	SO_3	P_2O_5	TiO_2	LOI
Dengban soil	42.7	13.63	12.6	7.15	4.53	3.06	1.18	0.21	0.18	0.68	14.1
Sand	51.66	7.32	9.21	2.54	2.53	1.32	2.14	0.08	0.3	0.29	4.56

Through mercury intrusion Porosimetry (MIP), the porosity and pore size distribution were measured using the AutoPore IV 9500 automatic mercury porosimeter, manufactured by Micromeritics Company. Samples were first dried in order to remove water from the pores. The dried samples were weighed and placed into a chamber, which had been evacuated to remove air from the samples. Mercury was then used to fill up the chamber. As the applied pressure was increased, mercury was forced to intrude into the samples gradually. The mercury intrusion volumes and the corresponding applied pressures were recorded at every pressure step. The mercury intrusion volume and the corresponding applied pressure provide the basic data for the analysis of pore structure.

3 Experimental Testing

3.1 Water Content

The mass of samples was measured by an electronic balance (with a measuring range of 4200 g and a precision of 0.01 g), and their size was measured by electronic vernier calipers (with a precision of 0.01 cm). An electro thermal blast drying oven was used to dry samples at 105 ± 2°C. Besides, samples were weighed every 3 h until the quality change was less than 2% according to GB/T 9966.3 [34]. This study improves the measurement precision by averaging the testing values of repeated measurements.

3.2 Specific Heat Capacity

The tested samples were in the absolute dry state (that is, their water content was 0%) to minimize the influence of moisture on the results. The classical mixing method is adopted: materials of a known mass are heated to a specific temperature and are put into the water of a specific mass at low temperatures. After the heat balance is reached, the heat values absorbed by the water and by the container are measured. The value of the heat equals the value of the heat released by the material. The specific heat of a material can be calculated as follows:

$$C = \frac{Q}{\Delta T \cdot m} \tag{1}$$

where Q is the heat absorbed or released by the sample (J), Δ_T is the temperature variation after the heat is absorbed or released by the sample (°C), m is the weight of the sample (kg), and C is the specific heat capacity of the sample (kJ/(kgK)).

The specific heat instrument applied in this study is the JPB-I heat capacity tester (Fig. 9a) developed by China Academy of Building Research and China Metrology Institute Dongfangaoda Co., Ltd., in Beijing. The instrument consists of an intelligent measuring instrument, a host, and a heating furnace. The test method applied was as follows: The sample was ground and dried in an oven at 75°C for 24 h. During the test, the specimen was put into the sample barrel, which was made of brass and was inserted into the temperature thermocouple, where the sample barrel's mass was measured. Then, the sample barrel was put into the heating furnace at 90°C with a temperature fluctuation of <1°C. The calorimeter was removed from the host, and its mass was weighed after drying. Then, pure water was poured into the host, and its mass was weighed. After that, the calorimeter was put back into the host again. After the temperature of the sample barrel was stabilized, the temperature was recorded in the 10^{th} minute, and the sample barrel was put back into the calorimeter. Then, the stirrer in the calorimeter was turned on when the water temperature in the calorimeter was increased. The temperature inside the calorimeter was recorded by the thermocouple every 10 seconds. When the water temperature started to decrease, the highest temperature was recorded for another 10 minutes. Consequently, the stirrer was stopped, and the test was finalized. HFP and CFP were respectively measured for six specimens, labeled as A-1~A-6 and B-1~B-6, respectively. Each specimen was measured three times, and the average values were taken.

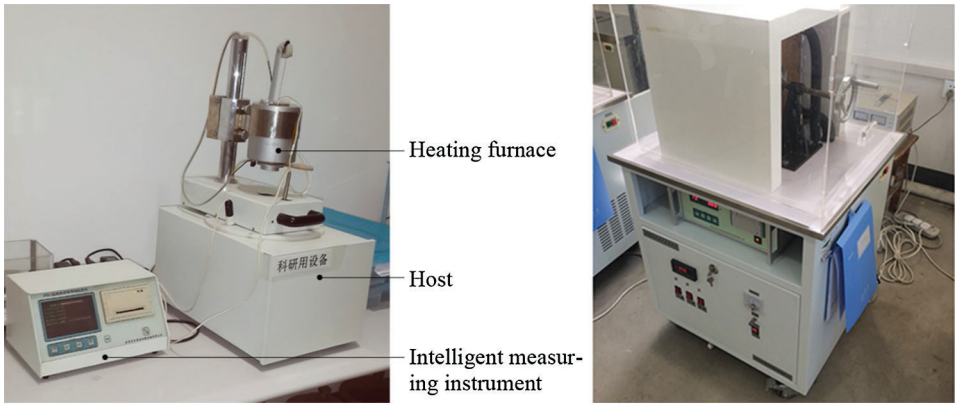

Figure 9: (a) JPB-I heat capacity tester; (b) JW-III thermal conductivity tester

3.3 Dry Thermal Conductivity

The heat flow meter method was used to measure the thermal conductivity of a material. Based on the relationship between the steady heat flow intensity, temperature, thermal conductivity, and thermal resistance, the thermal conductivity of a sample can be calculated as follows [35]:

$$R = \frac{t_1 - t_2}{q} \tag{2}$$

$$\lambda = \frac{d}{R} \tag{3}$$

where q is the heat transferred through unit area in unit time (W/m^2), t_1 and t_2 are the temperatures on both sides of the wall (K), d is the thickness of the sample (m), R is the thermal resistance of the sample (m^2K/W), and λ is the thermal conductivity of the sample (W/mK).

JW-III thermal conductivity tester (Fig. 9b) also consists of three parts: the host, the intelligent measuring instrument, and the cold and heat source control. The host consists of a hot plate, cold plate, and heat flowmeter. Six specimens with dimensions of 30 × 30 × 3 cm were prepared and designated as A-1~A-6 and B-1~B-6, respectively. Each specimen was measured three times, and the average values were taken. Before the test, specimens were dried in an electric drying oven at 75°C until a constant weight. Then, the sides of all the specimens were wrapped with four layers of plastic films, and the water vapor permeability resistance of the film was Sd > 1.5 m, which is considered to be airtight. The thickness and thermal resistance of the film were 0.0225 mm and 0.000537 m^2K/W, respectively; therefore, the subtle errors could be ignored. The mass of specimens was measured before and after each test to avoid the non-negligible influence of the water content. The dried specimen was placed in two flat plates parallel to each other at a constant temperature. In the steady-state, the heat flowmeter and the measuring portion of the specimen had one-dimensional constant heat flow. At such a steady-state, the thermal flow density, the value of the surface temperature, and the cold and hot plate output were measured by heat flowmeter to calculate the thermal resistance R. When the thickness of the specimen was input, the thermal conductivity of the material (λ) can be calculated.

3.4 Water Vapor Permeability

The water vapor permeability characterizes the ability of a material to transfer moisture under a vapor pressure gradient upon reaching the steady-state. It was measured as follows: First, the vapor partial pressure

on both sides of the material was controlled; then, the amount of water vapor transmitted through a specific size of the test piece was measured per unit time; finally, the vapor permeability coefficient was calculated. Water vapor permeability was tested in accordance with the standard [36] using the dry cup method. The sample was embedded at the top of the plastic container; it contained adequate desiccants, with anhydrous calcium chloride with a particle size of less than 3 mm, to maintain a stable RH level of 0% at 23°C. The distance between the upper surface of the desiccants and the lower surface of the sample was 20 mm, thereby avoiding the direct contact between the desiccants and the sample and enabling the forced flow of water vapor to pass through the sample only (Fig. 10). The sealed testing cup was maintained in a chamber at a constant temperature (23 ± 0.5°C) and RH (50 ± 3%) for the whole testing time (15 days for each sample), and weighed every 24 h. A total of 12 different samples (50 × 50 × 10 mm) were used.

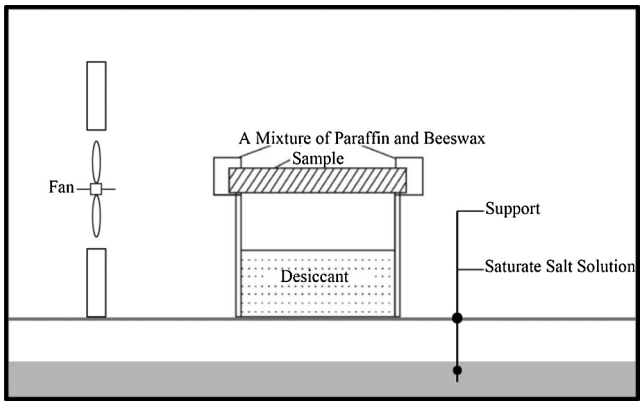

Figure 10: Experimental equipment for determining water vapor permeability

The water vapor resistance factor (μ) corresponding to the ratio of the water vapor permeability of the sample exceeded the water vapor permeability of air. The water vapor resistance factor has no unit. Therefore, if the water vapor resistance factor of a material is 5, then compared with the corresponding material under the same conditions, its resistance to water vapor diffusion will be five times its resistance to air diffusion [37].

The assembly mass was recorded until the constant time variation of mass ($\frac{\Delta m}{\Delta t}$) was achieved. The vapor pressure gradient between the climatic chamber environment and the cup (Δp) was estimated. For each specimen, the water vapor permeability (δp) was calculated according to the following equation:

$$\delta_p = \frac{\frac{\Delta m}{\Delta t}}{A \cdot \Delta p \cdot L} \tag{4}$$

where δp is the water vapor permeability (kg/(Pa·s·m)), Δm is the increased mass of the sample (kg), Δt is the constant time (s), A is the surface area of the sample (m^2), and L is the thickness of the sample (m).

The water vapor resistance factor (μ) was estimated as the following:

$$\mu = \frac{D}{\delta_p} \tag{5}$$

where μ is the water vapor resistance factor (-), and D is the water vapor permeability in the air (kg/(Pa·s·m)).

3.5 Equilibrium Moisture Content (EMC) and Sorption Isotherms

The hygroscopic behavior is the cause of the dilatation and shrinkage of materials, leading to cracks and bursts in buildings. The sorption isotherms were determined by the method of saturated salt solutions [38]. Relative humidity (RH) (given in percentage) is the ratio between the water vapor present and the air's saturation point, a value that changes with temperature. Equilibrium moisture content (EMC) is the moisture content at which a material is neither gaining nor losing moisture under certain environmental air conditions. It is a dynamic equilibrium that changes with relative humidity and temperature. Sorption isotherms revealed the relationship between RH and EMC in the material at a specified temperature. Earthen plaster samples were used with dimensions of 50 × 50 × 10 mm that were previously dried in a ventilated oven at 105°C until reaching a constant weight. Then, the specimens were placed in the glass desiccator with a defined RH at a constant temperature until the static sorption equilibrium was attained. The EMC was reached when the material neither gained nor lost water. The moisture content could be determined by Eq. (6):

$$MC = \frac{W_m - W_d}{W_d} * 100\% \tag{6}$$

where MC is the moisture content of the sample, W_m is the moisture weight (g), and W_d is the dry weight (g). A series of RH including 11.3%, 32.8%, 43.2%, 52.9%, 75.3%, 84.3%, and 97.3% RH were used for the tests. Besides, different RH levels in the glass desiccators were achieved by saturated salt solutions (Tab. 3). The dried specimens were placed on the plastic meshes over airtight containers containing various saturated salt solutions from low to high, respectively. The airtight containers were placed inside a chamber at 20°C and 60% RH. The samples were weighed at weekly intervals at least until the variation of two successive results showed a mass difference of less than 0.1%. When the tested samples reached a moisture equilibrium at 93.58% RH, the adsorption tests were terminated. Three specimens for each type of earthen plasters were used in different environments during the absorption phase.

Table 3: Saturated salt solutions used for adjusting different RH (20°C) [38]

Name	Molecular formula	Relative humidity (%)
Lithium chloride	LiCl	11.3 ± 0.3
Magnesium chloride	$MgCl_2{\cdot}6H_2O$	32.8 ± 0.2
Potassium carbonate	K_2CO_3	43.2 ± 0.4
Magnesium nitrate	$Mg(NO_3)_2$	52.9 ± 0.2
Sodium chloride	NaCl	75.3 ± 0.1
Potassium chloride	KCl	84.3 ± 0.1
Potassium sulfate	K_2SO_4	97.3 ± 0.5

4 Results and Discussions

4.1 MIP Analysis

The true density and apparent density of all the plaster samples were experimentally evaluated. In general, the characteristics were similar between the two types of samples despite a slight difference. The true density of HFP was 2238.81 kg/m^3 and it was 2336.45 kg/m^3 for CFP. This might be explained by the difference of both pore size and shape inside the matrix. As shown in Tab. 4, compared with HFP, the specific surface area of the pores in CFP is larger, while the pore diameter and porosity are smaller. The structure and size of the pores seriously affect the thermal conductivity and water absorption properties of the material.

Table 4: Results of mercury intrusion method

	HFP	CFP
Porosity/[%]	33.42	25.12
True Density [kg/m^3]	2238.81	2336.45
Apparent density (kg/m^3)	1537.21	1766.83
Average Pore Diameter/[nm]	149.6	109.0
Total Pore Area/[m^2/g]	6.43	10.27

As shown in Fig. 11a, the cumulative mercury intrusion for both the HFP or CFP, changes with the mercury intrusion pressure in a similar manner, such that the value gradually increases with pressure. As the mercury intrusion pressure increases, mercury is gradually pressed into the pores, which becomes smaller and smaller. When the pressure reached the maximum value of 33000 psia, the cumulative mercury intrusion of the sample was 0.282 and 0.245 ml/g for HFP and CFP, respectively. Due to differences in the pore structure (the existence form of pores and the porosity of the pores) between the HFP and CFP, the cumulative mercury intrusion of each sample is different under the same mercury intrusion pressure, which indicates that for different sample types, the porosity of the pores significantly varies. The values suggest that the HFP has a greater porosity than the CFP. The mercury intrusion and mercury removal curves of the samples do not overlap, indicating that there are ink bottle-shaped porosities, residual porosities, and other porosities in the samples with poor connectivity.

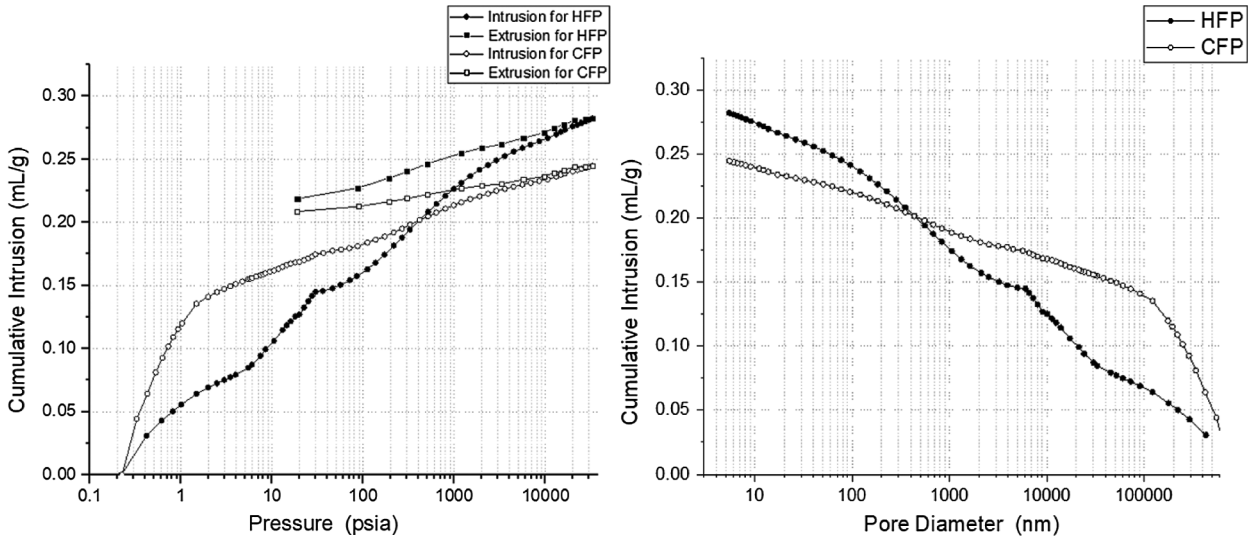

(a) (b)

Figure 11: (a) Cumulative mercury intrusion–distribution curve of mercury intrusion pressure. (b) Cumulative mercury intrusion–pore diameter distribution curve

As shown in Fig. 11b, when the two samples have the equal mercury intrusion pore size, their cumulative mercury intrusion values are also significantly different. When the mercury intrusion pore size is the same, more accumulated mercury means increased pore content (higher than the porosity) in soft soils. When the mercury intrusion pore size is 50000 nm, the cumulative mercury intrusion for CFP reaches 0.151 mL/g, while the cumulative mercury intrusion for HFP is only about half of the CFP value at 0.078 mL/g. This suggests that the content of large porosity in CFP pores is far greater than in HFP.

4.2 Water Content

The test results of water content are shown in Tab. 5. It is well-known that the water content directly affects the state of the earthen plasters. As the water content increases, the soil changes from solid-state to semi-solid state and then to plastic state, ultimately turning into a fluid state. When the earthen plasters were produced, it was mixed with a suitable amount of water to obtain a plastic state. Then, it was applied to the rock wall under the action of external force. After the internal moisture slowly evaporated, the earthen plasters became solid or semi-solid. As a result, the earthen plasters gained high strength and adhesion.

Table 5: Water content of samples

Sample	Water content ω (%)	
	M (Mean)	RSD (Relative standard deviation)
HFP	2.69	0.33
CFP	0.63	0.42

4.3 Dry Thermal Conductivity and Specific Heat Capacity

The values of dry thermal conductivity and specific heat capacity are presented in Fig. 12. The testing results showed that the average dry thermal conductivity of HFP and CFP was 0.183 W/mK with RSD of 1.67% and 0.218 W/mK with RSD of 1.28%, respectively. On the other hand, the average specific heat capacity of HFP and CFP was, respectively, 689 J/(kgK) (with RSD of 1.71%) and 709 J/(kg K) (with RSD of 1.55%). It should be noted that the RSD values of all the testing results were less than 5%, indicating a low dispersion degree.

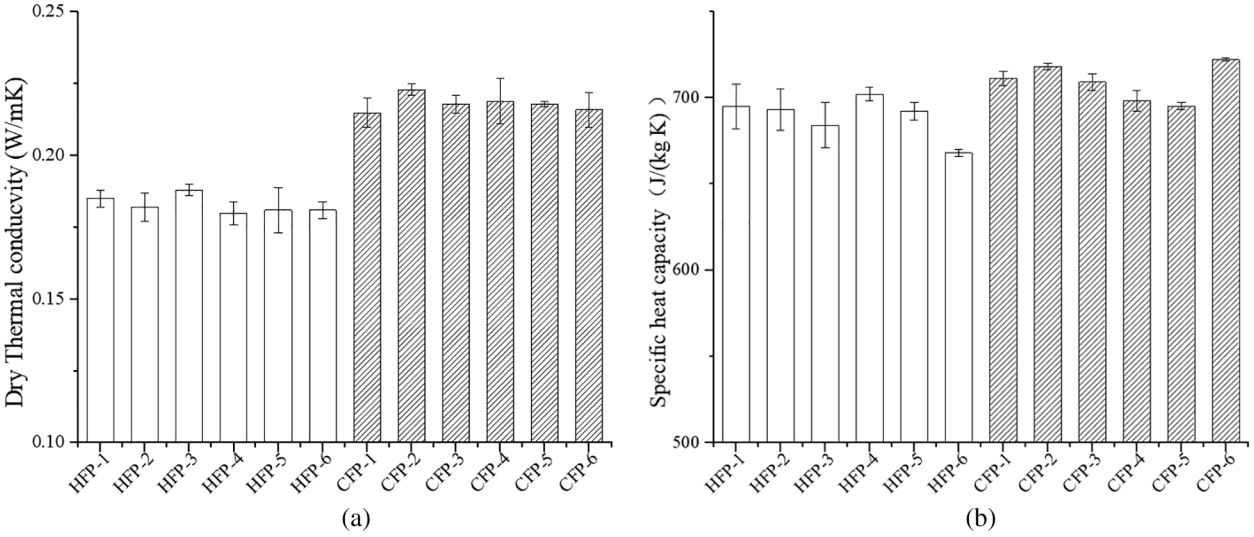

Figure 12: (a) Dry thermal conductivity and (b) specific heat capacity of the tested samples

The dry thermal conductivity of HFP was slightly lower than that of CFP. The earthen plasters was a porous material and consisted of solid phase and entrapped air after drying. The plaster with high density has few pores, which were filled with air at the dry state, and the thermal conductivity value of air is considerably lower than the solid phase. The solid phase was a mixture of Dengban soil, sand, and natural fibers. The entrapped air had a rather low thermal conductivity of about 0.026 W/mK. With the

increase of the density, the number of plant fibers per unit volume increased, while the porosity of samples and the pore size between fibers decreased. Because of the close contact of fibers, the solid thermal conductivity and thermal contact conductivity of both fibers increased. This effect became the main heat transfer mode of samples, increasing their thermal conductivity. Therefore, the CFP with higher density has higher thermal conductivity than the HFP with lower density.

No significant differences in specific heat capacity were observed between the samples at different fibers. The average of these two types of samples was rather close: 689 J/(kgK) for HFP and 709 J/(kgK) for CFP. Generally, the specific heat capacity of the sample depends on the proportion of solid phase, gas phase and liquid phase. The higher the specific heat capacity of the solid phase, the greater the specific heat capacity of the sample. Peng et al. [39] reported that the specific heat capacity of dry sand and dry soil was about 790 J/(kgK) and 840 J/(kgK), respectively. In this study, the soil and sand were mixed with 3% of plant fiber in a mass ratio of 100:3, which was likely to reduce the specific heat capacity.

4.4 Water Vapor Permeability

Tab. 6 shows the average values of water vapor permeability (δ_p) and the water vapor resistance factor (μ) of the two types of samples. It can be seen that all the samples had a relatively high resistance to water vapor. The average value of μ was 17.07 for HFP and 20.35 for CFP, indicating a poor water vapor permeability. The results were consistent with the experimental results in previous research [40]. Such a low water vapor permeability may be conducive to reducing the total deposition of soluble salts on the mural surface by reducing the water vapor in the earthen plasters.

Table 6: Water vapor resistance factor

Sample	Water vapor permeability δ_p [$\times 10^{-11}$ kg/(Pa·s·m)]	Water vapor resistance factor μ [-]
HFP	1.15	17.07
CFP	0.96	20.35

Water vapor could enter porous materials through pore openings at the surface, while liquid water inside the material could evaporate. The granular skeleton of the material reduced the available cross-sectional area of the air used for vapor diffusion. The complex spatial connectivity of the pore spaces increased the path length, thereby increasing additional water vapor resistance [41,42]. Although the coarse plaster of the samples was the same, the pore structures of the fine plaster were different due to the addition of different fibers. Fig. 12 showed that the pore size of the fine cotton plaster was smaller than that of the fine hemp plaster, thereby leading to the diverse transferability of water molecules in the two types of samples.

On the other hand, the density of cotton fiber was lower than that of hemp. Thus, at a fixed weight percentage, the added volume of cotton fiber would be larger than that of hemp, thereby resulting in a greater impact on the macro-porosity of the samples. Basically, the water vapor resistance of HFP (with hemp in the fine plaster) was lower than that of CFP (with cotton in the fine plaster).

Fig. 13 demonstrated how the water vapor resistance factor of earthen materials varied with their density. Liuzzi et al. [9] measured a similar μ of olive-fiber plasters in the order of μ ~22.1–25.0, which was higher than that of the experimental plasters in Mogao Grottoes. In a previous work [37], the results of the water vapor permeability test for different earthen plasters were found to be dependent on the density and the amount of water used during the sample preparation. Nevertheless, Liuzzi et al. observed a similar trend of the water vapor resistance factor by varying the density. In this study, however, the variation of the

water vapor resistance factor could not be explained solely by the varied density due to the limited number of samples and a low correlation.

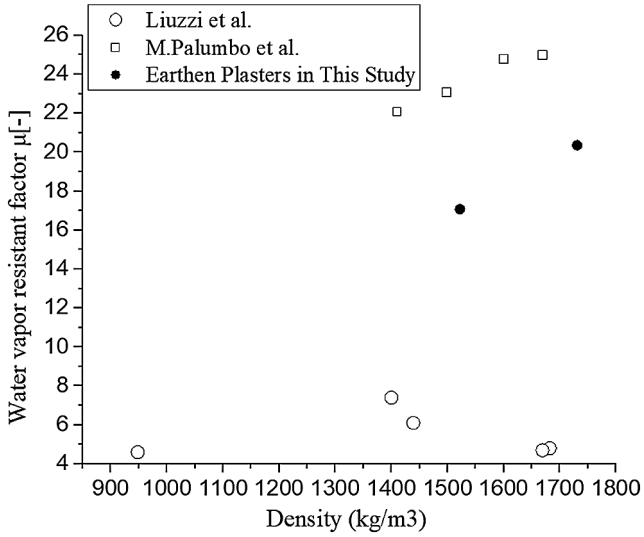

Figure 13: Plots showing the water vapor resistance factor against density for earthen materials

4.5 EMC and Sorption Isotherms

4.5.1 EMC

The equilibrium sorption moisture values collected during the measurement process (lasting about 50 days) were used to produce the sorption isotherms for the studied plasters. Fig. 14 shows the relationship between the EMC of the plaster samples and the RH at 20°C. Apparently, the EMC of the plaster samples increased with increasing the RH. It can be also seen that the EMC change ranges were 0.15%–26.75% (kg/kg) for HFP and 0.07%–1.75% (kg/kg) for CFP within the RH range of 11.3–97.3%, respectively. The results indicated that the EMC was less than 2% for both the two types of earthen plasters at an RH of below 52.9%. This helps to explain why plaster materials are useful for straw bale buildings for protecting the murals against harsh external conditions.

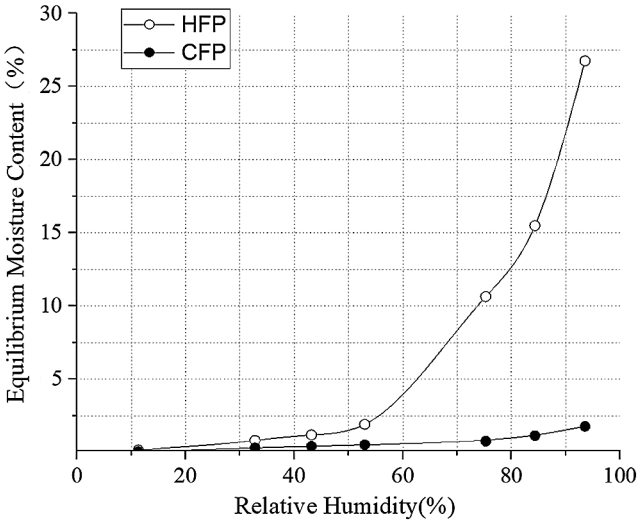

Figure 14: Relationship between RH and EMC for the analyzed samples

The EMC of HFP was higher than that of CFP. For HFP, the EMC increased much slower with increasing the RH to 52.9%, and further increasing the RH led to a more significant increase in the EMC. As for CFP, the increase in the EMC was less noticeable with gradually increasing the RH. For example, only a 1.3% increase in the moisture content was observed for CFP by increasing the RH from 52.9% to 84.3%, while the corresponding increase was 13.6% for HFP. Interestingly, within the high RH region, the change in the EMC varied more dramatically for the two types of samples, indicating that the material was more hygroscopic under a high humidity condition. These results revealed that the components in the plaster materials exerted a dominant influence on the sorption moisture. Compared with CFP, HFP gained significantly higher sorption moisture values at each RH. This could be attributed to the involvement of different fibers, which changed the pore structures inside the matrix. The two fibers have moisture absorption properties. As shown in Fig. 5, the two fibers are porous materials, and the incompleteness of the cellulose deposition results in a special structure called lumen, which can improve the hygroscopicity of fibers. At the microscopic level, the lumen of hemp fiber is larger than that of cotton fiber, which leads to more water absorption and storage in HFP at a high level of RH. Two mechanisms are responsible for this sorption phenomenon. At low RH, water molecules in the air are attracted to the hydrophilic groups of the fibrous macromolecules and then attach to the pore walls to form a thin water film. As the RH increases gradually, this water film becomes thicker, and the capillary condensation takes place in narrow pores. The two mechanisms may be at play at the same time; however, at high RH, the capillary condensation plays a dominant role. The above findings also indicate that RH in the caves should be kept below 52.9%, which is in line with the recommendation by Maekawa et al. [43].

4.5.2 Sorption Isotherms

The average EMC of the samples was calculated accordingly, and several regression curves were tested. In Díaz et al. [44], three theoretical models were used to represent the sorption isotherms for different materials. However, the Kumaran model (see Eq. (7)) and the Burch model (see Eq. (8)) gave more satisfactory results. Another model, known as the modified GAB model (see Eq. (9)), has also been widely used, which is based on the moisture content.

$$\mu = \frac{\psi}{a\psi^2 + b\psi + c} \tag{7}$$

$$\mu = a \cdot \left(\frac{1}{1-\psi} - 1\right)^b \tag{8}$$

$$\mu = \frac{C_G \cdot k \cdot \psi}{(1 - k \cdot \psi)(1 - k \cdot \psi + C_G \cdot k \cdot \psi)} w_m \tag{9}$$

where μ is the moisture content, ψ is RH, and a, b, c, C_G, k, and w_m are constants.

The relationship between EMC and RH was not linear, as can be seen in Fig. 15. The model parameters for all models are shown in Tab. 7. The correlation coefficients were higher than 0.960 in all cases, indicating that the models fitted reasonably well with the measurements. For HFP, the best-fitting results were obtained by the Kumaran model, while the Burch model provided the closest results for CFP. A previous study showed that the GAB model was suitable to fit the experimental data of the plasters reinforced with barley straw, wheat straw, and wood shavings, and plasters without fiber as a function of both temperature and RH [45]. The GAB model was suitable to predict the data for plasters reinforced with several different fibers.

Two types of fibers-hemp fiber and cotton fiber-were used in fine layers of the two types of samples. The results showed that there was little difference in thermal performance but significant difference in hygric properties between these two types of samples. Compared with CFP, HFP had better permeability

to water vapor and thereby could absorb more water vapor at any fixed RH. In other words, water permeated more quickly in HFP than in CFP. Hence, under the same condition, more water and salt were able to migrate to the surface of murals prepared with HFP. Therefore, the HFP incorporated murals are more vulnerable to diseases.

The CFP had a relatively low dry thermal conductivity, a weak ability to transfer water vapor, and a high storage capacity for heat and moisture. All these features are beneficial to the long-term preservation of murals. It acts as a cushion layer against the effect of temperature waves and humidity change on the paint layer. A poor permeability to water can reduce the rate of water transfer and prevent salt from transferring water to the mural surface. On the other hand, lower dry thermal conductivity alleviates the damages to murals caused by changes in ambient temperature.

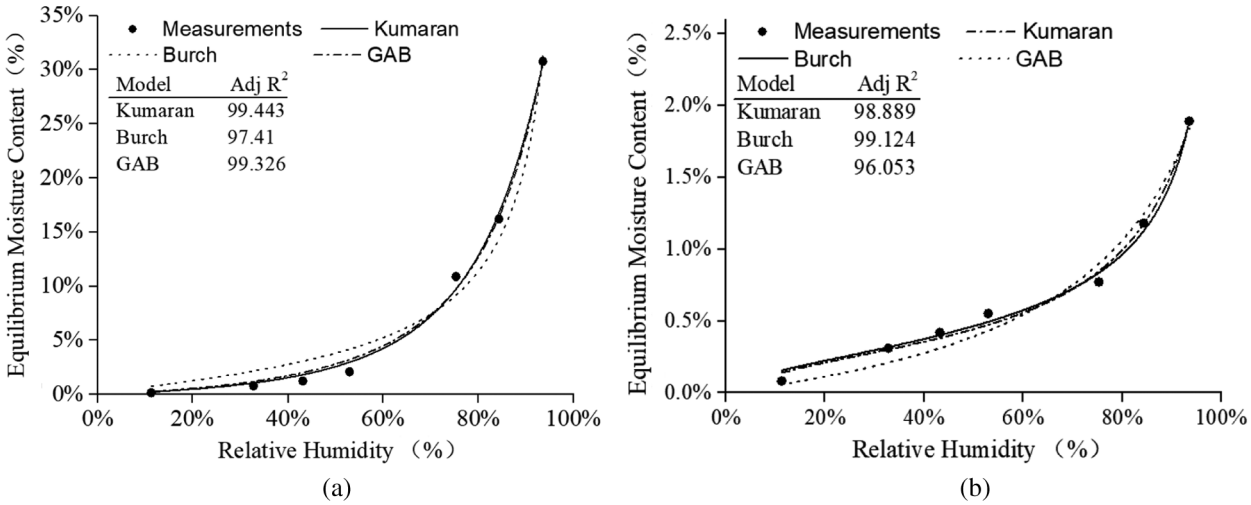

Figure 15: Comparison of three regression curves for sorption of (a) HFP and (b) CFP

Table 7: Specific function expressions and error

Model	Sample	Constants	Adj R^2
Kumaran model	HFP	$A = 47.52$, $b = -105.89$, $c = 60.52$	0.994
	CFP	$A = -276.81$, $b = 252.91$, $c = 55.42$	0.989
Burch model	HFP	$A = 0.038$, $b = 0.789$	0.974
	CFP	$A = 0.004$, $b = 0.526$	0.991
GAB model	HFP	$C_G = 0.011$, $k = 0.809$, $w_m = 2.358$	0.993
	CFP	$C_G = 10.101$, $k = -0.091$, $w_m = -0.005$	0.961

5 Conclusions

From the results, it appears that the reinforcement of two natural fibers (hemp and cotton fiber) has much more impact on the hygric properties (water vapor permeability and sorption isotherms) of earthen plasters than on their thermal performance (specific heat capacity and dry thermal conductivity).

The thermal conductivity of earthen plasters increased with increasing density. The CFP with higher density has higher thermal conductivity than the HFP with lower density. This might be explained by the difference of both pore size and shape inside the matrix. But no significant differences of specific heat

capacity were observed between the samples at different fibers. Compared with CFP, HFP had better permeability to water vapor and was able to absorb more water vapor at any given RH, indicating that water vapor permeates more quickly and more water is retained in HFP than in CFP.

The overall findings highlight that all these features of CFP are beneficial to the long-term preservation of murals. The CFP used in murals can reduce the rate of water transfer and prevent salt from transferring water to the mural surface. It can also alleviate the damages to murals caused by changes in ambient temperature. The earthen plasters in Mogao functions as a cushion layer against the effect of temperature waves and humidity change on the paint layer. The study of the earthen plasters in Mogao Grottoes is of general significance. This multi-layer structure of murals exists not only in Mogao Grottoes but also in caves, tombs, palaces, and temples around the world. This paper sheds new insights into the study of the earthen plasters in other cultural relics. Moreover, the measured properties can be used to obtain coupled heat and moisture analysis of the earthen plasters and to dissect the degradation mechanism of murals.

Acknowledgement: We thank Papergoing (http://www.papergoing.com) for editing this manuscript. We also thank Dr. Mingzhi Guo for his help on the quality of language.

Funding Statement: This project was supported by the National Natural Science Foundation of China (Projects No. 51378412) and China State Administration of Cultural Heritage (Project No. 20110308).

Conflicts of Interest: The authors declare that they have no conflicts of interest to report regarding the present study.

References

1. Li, Z. X. (2003). *The silk road grotto fresco statues preservation*. China: Science Press.
2. Randazzo, L., Montana, G., Hein, A., Castiglia, A., Rodono, G. et al. (2016). Moisture absorption, thermal conductivity and noise mitigation of clay based plasters: the influence of mineralogical and textural characteristics. *Applied Clay Science, 132–133,* 498–507. DOI 10.1016/j.clay.2016.07.021.
3. Zhang, L., Yang, L., Jelle, B. P., Wang, Y., Gustavsen, A. et al. (2018). Hygrothermal properties of compressed earthen bricks. *Construction and Building Materials, 162,* 576–583. DOI 10.1016/j.conbuildmat.2017.11.163.
4. Santos, T., Maria, I. G., António, S. S., Ferraz, E., Faria, P. (2020). Comparison of mineralogical, mechanical and hygroscopic characteristic of earthen, gypsum and cement-based plasters. *Construction and Building Materials, 254,* 119222–119232. DOI 10.1016/j.conbuildmat.2020.119222.
5. Sathiparan, N., Rupasinghe, M. N., Pavithra, B. H. M. (2017). Performance of coconut coir reinforced hydraulic cement mortar for surface plastering application. *Construction and Building Materials, 142,* 23–30. DOI 10.1016/j.conbuildmat.2017.03.058.
6. Gourlay, E., Glé, P., Marceau, S., Foy, C., Moscardelli, S. (2017). Effect of water content on the acoustical and thermal properties of hemp concretes. *Construction and Building Materials, 139,* 512–523. DOI 10.1016/j.conbuildmat.2016.11.018.
7. Belayachi, N., Hoxha, D., Slaimia, M. (2016). Impact of accelerated climatic aging on the behavior of gypsum plaster-straw material for building thermal insulation. *Construction and Building Materials, 125,* 912–918. DOI 10.1016/j.conbuildmat.2016.08.120.
8. Page, J., Khadraoui, F., Boutouil, M., Gomina, M. (2017). Multi-physical properties of a structureal concrete incorporating short flax fibers. *Construction and Building Materials, 140,* 344–353. DOI 10.1016/j.conbuildmat.2017.02.124.
9. Liuzzi, S., Rubino, C., Stefanizzi, P., Petrella, A., Boghetich, A. et al. (2018). Hygrothermal properties of clayey plasters with olive fibers. *Construction and Building Materials, 158,* 24–32. DOI 10.1016/j.conbuildmat.2017.10.013.
10. Lima, H. C., Willrich, F. L., Barbosa, N. P., Rosa, M. A., Cunha, B. S. (2008). Durability analysis of bamboo as concrete reinforcement. *Materials and Structures, 41(5),* 981–989. DOI 10.1617/s11527-007-9299-9.

11. Mazhoud, B., Collet, F., Pretot, S., Chamoin, J. (2016). Hygric and thermal properties of hemp lime plasters. *Building and Environment, 96,* 206–216. DOI 10.1016/j.buildenv.2015.11.013.
12. Duan, X. Y. (1988). Understanding of the materials for making murals in Mogao grottoes. *Dunhuang Research, 3,* 41–60.
13. Zhao, L. Y., Li, Y. F., Yu, Z. R., Li, Z. X. (2005). Silk Road grotto fresco plaster making materials and process analysis. *Dunhuang Research, 004,* 75–82. DOI 10.3969/j.issn.1000-4106.2005.04.014.
14. Mwaikambo, L. Y., Ansell, M. P. (2003). Hemp fibre reinforced cashew nut shell liquid composites. *Composites Science and Technology, 63(9),* 1297–1305. DOI 10.1016/S0266-3538(03)00101-5.
15. Madsen, B., Lilholt, H. (2003). Physical and mechanical properties of unidirectional plant fibre composites–An evaluation of the influence of porosity. *Composites Science and Technology, 63(9),* 1265–1272. DOI 10.1016/S0266-3538(03)00097-6.
16. Jiang, Y., Lawrence, M., Ansell, M. P., Hussain, A. (2018). Cell wall microstructure, pore size distribution and absolute density of hemp shiv. *Royal Society Open Science, 5(4),* 171945. DOI 10.1098/rsos.171945.
17. Shahzad, A. (2012). Hemp fiber and its composites—a review. *Journal of Composite Materials, 46(8),* 973–986. DOI 10.1177/0021998311413623.
18. Şükrü, Y., Özlem, Ç., Ahmet, Ç (2008). The effects of the fiber contents on the mechanic properties of the adobes. *Construction and Building Materials, 22(3),* 222–227. DOI 10.1016/j.conbuildmat.2006.08.022.
19. Anders, T., Geoffrey, D., Hans, L., Anne, B. T. (2006). Hemp fiber microstructure and use of fungal defibration to obtain fibers for composite materials. *Journal of Natural Fibers, 2(4),* 19–37. DOI 10.1300/J395v02n04_02.
20. Zhang, J. C., Zhang, H. (2008). Structure and performance of hemp fibre and process technology. *Polymer Bulletin, 12,* 46–53.
21. Wang, Y. P., Gao, X. S., Xing, S. Y., Geng, L., Zhang, X. D. (2006). Structure research of several natural cellulose fibers. *Cotton Textile Technology, 2,* 12–16.
22. Evin, C. (2003). *Archaeometrical investigation of some seljuk plasters (Ph.D. Thesis)*. The Middle East Technical University, Turkey.
23. Agnew, N., Maekawa, S., Wei, S. (2010). Causes and mechanisms of deterioration and damage in cave 85. In: Agnew, N. (eds.) *Conservation of Ancient Sites on the Silk Road: Proceedings of the Second International Conference on the Conservation of Grotto Sites,* Mogao Grottoes, Dunhuang, China, pp. 412–420. Los Angeles, California, United States: The Getty Conservation Institute.
24. Xu, X., Zhang, L., Chen, L., Liu, C. (2020). The role of soil N2O emissions in agricultural green total factor productivity: an empirical study from china around 2006 when agricultural tax was abolished. *Agriculture, 10 (5),* 150. DOI 10.3390/agriculture10050150.
25. Li, Z. X. (2010). Deterioration and treatment of wall paintings in grottoes along the silk road in china and related conservation efforts, first progress report in conservation of ancient sites on the silk road. *Proceedings of the Second International Conference on the Conservation of Grotto Site,* Mogao Grottoes, Dunhuang, China, pp. 46–55. The Getty Conservation Institute, Los Angeles.
26. Zhang, M. Y., Zhang, H. Y., Zeng, Z. Z. (1995). Mechanism of salt efflorescent disease in murals of Mogao Grottoes. *Journal of Lanzhou University, 1,* 96–101.
27. Guo, Q. L. (2009). *Origin of water and salts responsible for wall paintings disease at dunhuang mogao grottoes (Ph.D. Thesis)*. Lanzhou University, China.
28. Lin, B., Wang, X. D., Guo, Q. L. (2013). A study on the variation laws of temperature and relative humidity in the rock of the west wall in mogao cave 108. *Dunhuang Research, 137,* 86–91.
29. Wang, J. L., Yan, Z. F., Wang, X. D., Zhang, Z. M., Shang, R. H. et al. (2016). Experimental research on mechanical ventilation system for cave 328 in mogao grottoes, Dunhuang, China. *Energy and Buildings, 130,* 692–696. DOI 10.1016/j.enbuild.2016.08.086.
30. Li, F. J., Wang, X. D., Guo, Q. L., Zhang, B., Pei, Q. Q. et al. (2019). Moisture adsorption mechanism of earthen plaster containing soluble salts in the mogao grottoes of China. *Studies in Conservation, 64(3),* 159–173. DOI 10.1080/00393630.2018.1537351.

31. Zhang, H. Y., Yan, G. S. (2012). Laboratory test on moisture adsorption-desorption of wall paintings at Mogao Grottoes, China. *Journal of Zhejiang University-SCIENCE A, 13(3),* 208–218. DOI 10.1631/jzus.A1100204.
32. Du, J., Xie, B., Liu, H., Chen, R. H. (2016). Study of the mechanical characteristics of the plaster ground samples of wall-paintings in the Mogao Grottoes. *Sciences of Conservation Archaeology, 6,* 55–62.
33. Sun, M. Y., Wang, J., Zhang, B. (2015). Measurement of the reversible rate of conservation materials for ancient murals. *Journal of Cultural Heritage, 16(1),* 49–56. DOI 10.1016/j.culher.2014.01.010.
34. GB/T 9966.3 (2001). *Test methods for natural facing stones—Part 3: test methods for bulk density, true density, true porosity and water content*. China: China Standard Press.
35. Sun, L. X. (2018). *Research on the long-term performance of stone wool ETICS under coupled heat and mass transfer impact (Ph.D. Thesis)*. Xi'an University of Architecture and Technology, China.
36. Bureau, N. T. S. (2015). *Test methods for water vapour transmission properties of building materials and products*. China: China Standard Press.
37. Palumbo, M., McGregor, F., Heath, A., Walker, P. (2016). The influence of two crop by-products on the hygrothermal properties of earth plasters. *Building and Environment, 105,* 245–252. DOI 10.1016/j.buildenv.2016.06.004.
38. GB/T 20312 (2006). *Hygrothermal performance of building materials and products determination of hygroscopic sorption properties*. China: China Standard Press.
39. Peng, Y. J., Peng, B. (2016). Analysis and calculation of soil thermal physical indicators. *Chinese Journal of Underground Space and Engineering, 12,* 38–43.
40. Su, B. M., Zhang, H. Y., Zhang, B. J., Jiang, D., Zhang, R. et al. (2018). A scientific investigation of five polymeric materials used in the conservation of murals in Dunhuang Mogao Grottoes. *Journal of Cultural Heritage, 31,* 105–111. DOI 10.1016/j.culher.2018.01.002.
41. Hall, M., Allinson, D. (2009). Analysis of the hygrothermal functional properties of stabilised rammed earth materials. *Building and Environment, 44(9),* 1935–1942. DOI 10.1016/j.buildenv.2009.01.007.
42. Xu, X., Zhang, C., Chen, L., Li, C. (2019). How does industrial waste gas emission affect health care expenditure in different regions of china: an application of bayesian quantile regression. *International Journal of Environment Research and Public Health, 16(15),* 2748. DOI 10.3390/ijerph16152748.
43. Maekawa, S., Liu, G., Xue, P., Guo, Q., Hou, W. (2004). Origins of moisture affecting the wall paintings in cave 85. In: Agnew, N. (eds.), *Conservation of Ancient Sites on the Silk Road. Second International Conference on the Conservation of Grotto Sites,* pp. 464–470. Mogao Grottoes Dunhuang, Gansu Province, China.
44. Díaz, J. J. D. C., Rabanal, F. P.Á., Nieto, P. J. G., Hernández, J. D., Soria, B. R. et al. (2013). Hygrothermal properties of lightweight concrete: experiments and numerical fitting study. *Construction and Building Materials, 40,* 543–555. DOI 10.1016/j.conbuildmat.2012.11.045.
45. Ashour, T., Georg, H., Wei, W. (2011). An experimental investigation on equilibrium moisture content of earth plaster with natural reinforcement fibres for straw bale buildings. *Applied Thermal Engineering, 31(2–3),* 293–303. DOI 10.1016/j.applthermaleng.2010.09.009.